

Formation of Oxygen Radicals in $12\text{CaO}\cdot 7\text{Al}_2\text{O}_3$: Instability of Extraframework Oxide Ions and Uptake of Oxygen Gas

Katsuro Hayashi,^{*,†} Satoru Matsuishi,^{†,‡} Masahiro Hirano,[†] and Hideo Hosono^{†,‡}

Transparent Electroactive Materials Project, Japan Science and Technology Agency, KSP C-1232, Kawasaki 213-0012, Japan, and Materials and Structures Laboratory, Tokyo Institute of Technology, Yokohama 226-8503, Japan

Received: December 18, 2003; In Final Form: March 24, 2004

The thermodynamics and kinetics of oxygen radical formation in cages of a nanoporous crystal, $12\text{CaO}\cdot 7\text{Al}_2\text{O}_3$, were examined during isothermal annealing in a dry oxygen atmosphere. The formation of oxygen radicals, O_2^- and O^- , involves the outward diffusion of extraframework oxide ions, their oxidation by absorbed oxygen molecules to form O^- and O_2^- at the surface, and subsequent inward diffusion of the oxygen radicals. The instability of the extraframework oxide ions provides the driving force for this process. Evaluating the radical formation enthalpy and entropy enabled us to determine the temperature and oxygen partial pressure dependences of equilibrium oxygen radical concentration. The rate-limiting process for the radical formation is not the surface reaction, but the total ionic diffusion process, in which the smaller diffusivity of O_2^- likely dominates the process.

I. Introduction

$12\text{CaO}\cdot 7\text{Al}_2\text{O}_3$ (C12A7)^{1–12} has unique features in its crystal lattice. The unit cell under stoichiometric composition, $2[\text{Ca}_{12}\text{Al}_{14}\text{O}_{33}]$, is represented as $[\text{Ca}_{24}\text{Al}_{28}\text{O}_{64}]^{4+}\cdot 2\text{O}^{2-}$. The former part, $[\text{Ca}_{24}\text{Al}_{28}\text{O}_{64}]^{4+}$, denotes a three-dimensional lattice framework with 12 cages and an inner free space ~ 0.4 nm in diameter. Thus, each cage has a mean effective charge of $+1/3$ ($= +4$ charges/12 cages). The latter part, 2O^{2-} , refers to free oxide ions, which occupy $1/6$ of the cage sites.¹ In oxidizing or inert gas atmospheres, C12A7 exhibits oxide ion conductivity within an order of magnitude smaller than that of yttria-stabilized zirconia and has an oxide ionic transference number of unity.² Thus, the free oxide ions are responsible for the fast oxide ion conduction.

It has been demonstrated that the free oxide ions can be partially or completely replaced by various monovalent anions such as OH^- ,³ F^- ,⁴ Cl^- ,⁴ O_2^- ,^{5–8} O^- ,^{6–8} and H^- .⁹ Furthermore, the electron can also act as a substitutional anion in strongly reducing conditions.¹⁰ To preserve charge neutrality, monovalent anions occupy $1/3$ of the cage sites and their maximum concentration is limited to $2.32 \times 10^{21} \text{ cm}^{-3}$. Among such anions, oxygen radical anions (O_2^- and O^-) are particularly important due to their high oxidation reactivity,^{16,17} which makes C12A7 attractive as an oxidation catalyst¹¹ or an oxide ion conducting solid electrolyte with catalytic activity. Further, oxygen radical-loaded C12A7 enables efficient electric-field extraction of the O^- radical in a vacuum,¹² which provides a novel method for generating a high-density O^- -ion beam.

Oxygen radical formation conditions have been investigated experimentally with respect to atmosphere and temperature. It was found that a higher concentration of oxygen radicals was favored in lower humidity⁶ and higher oxygen pressure⁸ and

the oxygen radical concentration changed abruptly in temperature range 500–800 °C.⁷ In the present study, the thermodynamics and kinetics of oxygen radical formation in a dry oxygen atmosphere are examined on the basis of isothermal annealing at 550–700 °C, which provides a clearer understanding of the oxygen radical formation process and an insight into the stable incorporation of such highly reactive species in C12A7.

II. Experimental Section

C12A7 ceramic samples were prepared by a solid-state reaction of CaCO_3 and $\gamma\text{-Al}_2\text{O}_3$ powders at 1350 °C for 6 h in dry oxygen ($p_{\text{O}_2} = 1 \text{ atm}$, $p_{\text{H}_2\text{O}} = 6 \times 10^{-5} \text{ atm}$). They were again heated at 1350 °C for 2 h in dry oxygen and then immediately transferred to a water-cooled zone of the tube furnace to quench the samples to room temperature. The resultant ceramics had $\sim 80\%$ of the theoretical density ($2.68 \text{ g}\cdot\text{cm}^{-3}$).⁴ The microstructure in fractured surfaces of the ceramic was observed by a scanning electron microscopy (SEM) after surfaces were coated with carbon by vacuum evaporation. Figure 2 shows a typical image. The estimated average grain size was $11 \pm 4 \mu\text{m}$. Samples were again placed at the cooled zone of the furnace under dry oxygen flow. They were quickly transferred to a hot zone heated to 700, 625, or 550 °C, held for times ranging from 2 min to 128 h, and then quenched to room temperature. The annealing procedures did not significantly change the microstructure.

Electron paramagnetic resonance (EPR) measurements were conducted at $\sim 9.7 \text{ GHz}$ (X-band), using a Bruker E580 spectrometer at 77 K. The spin concentrations in samples were determined from the second integral of the spectrum, using $\text{CuSO}_4\cdot 5\text{H}_2\text{O}$ as a standard, which provided an accuracy of $\pm 20\%$. Raman spectra were measured with a Fourier transformation (FT)-Raman spectrometer at room temperature, using a YAG laser ($\lambda = 1.064 \mu\text{m}$) as an excitation light source.

* Author to whom correspondence should be addressed. E-mail: k-hayashi@net.ksp.or.jp.

[†] Japan Science and Technology Agency.

[‡] Tokyo Institute of Technology.

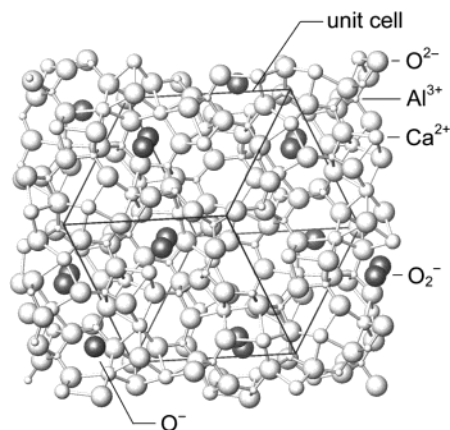


Figure 1. Crystal structure of C12A7 viewed along the nearly (111) direction. The lattice framework is indicated by white spheres (Ca^{2+} , Al^{3+} , and O^{2-} ions) bonded by white rods. The black frame indicates the cubic unit cell with a lattice constant of 1.199 nm. The oxygen radicals (O_2^- and O^-) are shown as isolated gray spheres. The depicted state corresponds to complete substitution of oxygen radicals for the extraframework O^{2-} ions.

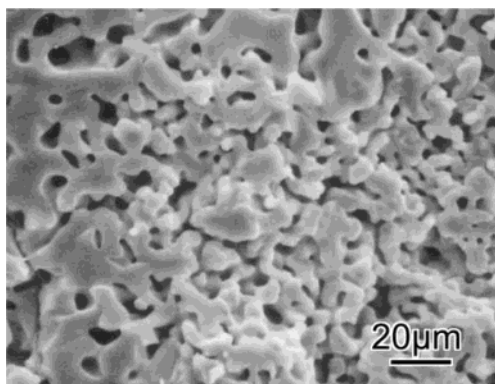


Figure 2. SEM image of a fractured surface of a sample sintered at 1350 °C for 8 h in dry oxygen.

III. Results

Figure 3 shows typical EPR and the Raman spectra. As shown in spectra 1 and 2, most of the EPR spectra were consistently analyzed by the superposition of calculated powder patterns for O_2^- and O^- with Lorentzian line shapes and g values, $g_{xx} = 2.002(\pm 0.001)$, $g_{yy} = 2.008(0.001)$, and $g_{zz} = 2.074(0.001)$ for O_2^- , and $g_{xx} = g_{yy} = 2.036(0.005)$ and $g_{zz} = 1.994(0.01)$ for O^- .^{6–8} The concentrations of O^- and O_2^- radicals were evaluated from the intensity ratio of calculated powder patterns giving best fit to the measured spectrum. When the total spin concentration was greater than $\sim 8 \times 10^{20} \text{ cm}^{-3}$, the spectral shape apparently lost the g -anisotropy due to the dipolar broadening and became a nearly single Lorentzian shape as in spectrum 3, where the separate evaluation of the individual radical concentrations is difficult. In these cases, the O_2^- concentration was evaluated from the intensity of the 1128-cm^{-1} Raman band as in Figure 3b, which is attributed to the O_2^- stretching mode.¹⁷ Then, the O^- concentration was determined by subtracting the O_2^- concentration from the total spin concentration obtained from EPR. Details of the above procedure have been described elsewhere.⁸ The samples did not show any trace of O_2 molecules, which give a Raman band at $\sim 1560 \text{ cm}^{-1}$.¹⁷

The estimated concentrations of O_2^- and O^- in the 1350 °C quenched sample were 2.8×10^{19} and $3 \times 10^{18} \text{ cm}^{-3}$, respectively. These concentrations correspond to a composition of ca. $\text{Ca}_{12}\text{Al}_{14}\text{O}_{33+0.07}$, in which $\sim 97\%$ of the free oxide ions

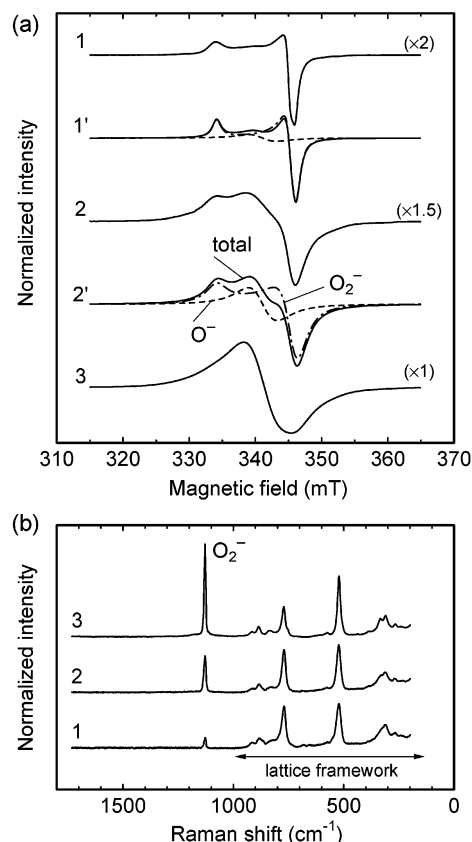
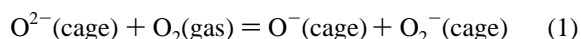


Figure 3. (a) EPR spectra of the samples annealed in dry oxygen (1) at 700 °C for 2 min, (2) at 625 °C for 1 h, and (3) at 550 °C for 16 h. Solid curves 1' and 2' are superpositions of the calculated powder patterns of O_2^- (point-dashed line) and O^- (dashed line) components. (b) Raman spectra of samples 1–3 in panel a.

remain in the cages. Thus, the 1350 °C quenched sample is nearly stoichiometric. Figure 4 shows the annealing time, t , dependence of the radical concentrations at 700, 625, and 550 °C. The total radical concentration at each temperature increases in proportion to $t^{1/2}$ in the initial stage and then saturates, reaching equilibrium. The equilibrium total concentration increases as the temperature decreases. Interestingly, annealing at 550 °C for > 32 h gives a total concentration as high as $1 \times 10^{21} \text{ cm}^{-3}$ without employing the high oxygen pressure of the previous study.⁸ This concentration corresponds to the chemical formula of ca. $\text{Ca}_{12}\text{Al}_{14}\text{O}_{33+1}$ and reduction of the remaining free oxide ions to $\sim 58\%$. The O^- concentration is always less than O_2^- , but the concentration ratio approaches 1:1 when the total radical concentration increases.

IV. Discussion

1. Equilibrium Concentration of Oxygen Radicals. The oxygen radical formation process is deduced from the following experimental observations: (1) a weight loss equivalent to desorption of incorporated oxygen was observed when the oxygen radicals were annihilated by heating in excess of 700 °C in a He atmosphere,¹³ and (2) nearly the same amount of O^- and O_2^- is simultaneously formed in stoichiometric C12A7 as has been observed previously.^{6–8} Thus, the major reaction for the oxygen radical formation is described by



i.e., an electron transfer from a free oxide ion to an oxygen molecule incorporated from the atmosphere into a cage.⁶ Isotopic

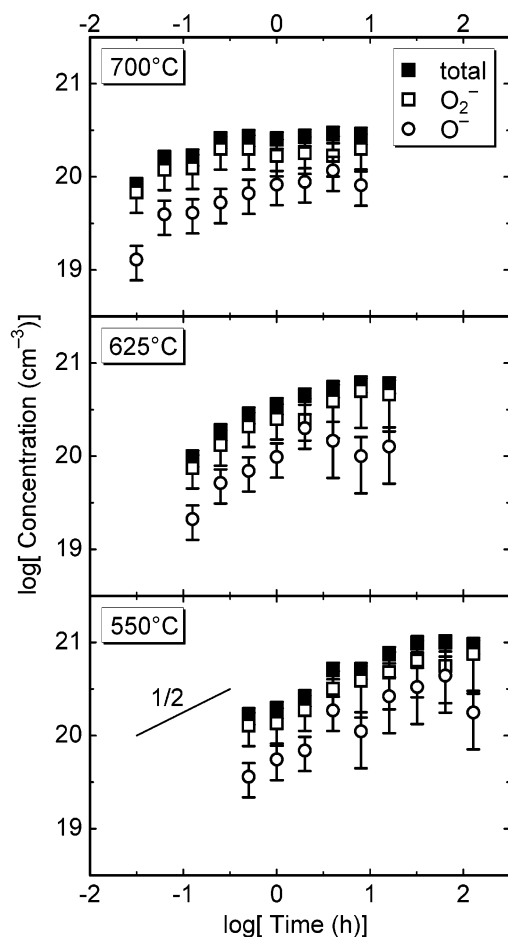


Figure 4. Changes in each oxygen radical (O^- , O_2^-) and the total radical concentrations as a function of annealing time at 700, 625, and 550 °C. Error bars originate both from the EPR measurements and the deconvolution of total EPR spectra into those of O^- and O_2^- .

experiments with ^{17}O further support eq 1 as the dominant process for forming the radicals.¹⁴ Discrepancy from the ideal formation ratio of O^- and O_2^- may be due to the additional interconversion reactions among O^{2-} , O^- , and O_2^- , or reactions with H_2O to form OH^- in cages. Further, O^- in the cage may be easier to annihilate than O_2^- since it is generally known that O^- is less stable than O_2^- when formed on the oxide surface.¹⁷ Similarity of the g_{zz} values¹⁶ of O^- and O_2^- incorporated into the cages to those of adsorbates on oxide surface supports this consideration.

The equilibrium constant, K , for eq 1 is described as

$$K = \frac{[O^-][O_2^-]}{[O^{2-}]p_{O_2}} \quad (2)$$

where all the chemical species are assumed as ideal solution and ideal gas. Brackets denote concentration in mole fractions. Occupancy of the free O^{2-} ion in stoichiometric C12A7 is 1 and thus $[O^{2-}] = 1$. When whole the free O^{2-} ions are reacted to form the oxygen radicals, inoccupation of O^{2-} ions ($[O^{2-}] = 0$) is compensated by the occupation of a pair of oxygen radicals ($[O^-] = [O_2^-] = 1$). These reactions together with the charge neutrality condition restricts the cage constituents

$$2[O^{2-}] + [O^-] + [O_2^-] = 2 \quad (3)$$

That is, to compensate for the positive charge of the lattice, one molecule of C12A7 should incorporate $2e^-$ of anion(s) in

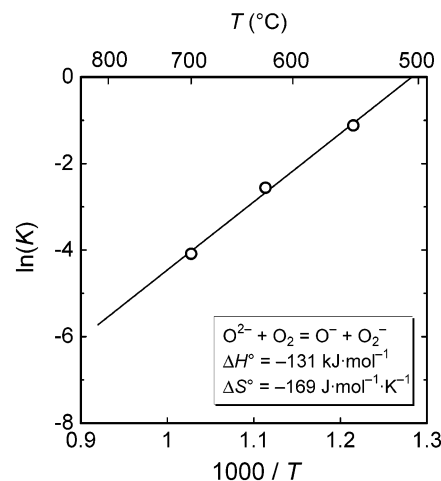


Figure 5. Arrhenius plot of the equilibrium constant (K).

TABLE 1: Enthalpy of Processes Concerning the Oxygen Radical Formation in the Gas Phase^a

		ΔH (kJ·mol ⁻¹)	ref
process		at 0 K	
i	$O_2 + e^- \rightarrow O_2^-$	-42.5	18, 19
ii	$O + e^- \rightarrow O^-$	-141	19–21
iii	$O^- + e^- \rightarrow O^{2-}$	844	21
iv	$O^{2-} + O_2 \rightarrow O^- + O_2^-$	-886.5	<i>b</i>
v	$O^{2-}(\text{cage}) + O_2(\text{gas}) \rightarrow O^-(\text{cage}) + O_2^-(\text{cage})$	-131 ^c	present study

^a Except process v, which includes the cage-incorporated state.

^b Calculated from processes i and iii. ^c 625 °C.

the cages independent of the oxygen radical concentrations. Provided that O^- and O_2^- are formed via reaction 1, each concentration is a half of the total radical concentration, $[O_x^-]$,

$$\frac{1}{2}[O_x^-] \cong [O_2^-] \cong [O^-] \quad (4)$$

Then, eq 2 is rewritten as

$$K = \frac{[O_x^-]^2}{2p_{O_2}(2 - [O_x^-])} \quad (5)$$

The temperature change of K is plotted in Figure 5, using the experimental value of equilibrium $[O_x^-]$. From the relationship

$$RT \ln K = T\Delta S^\circ - \Delta H^\circ \quad (6)$$

The enthalpy (ΔH°) and the entropy (ΔS°) for eq 1 at ~625 °C (the center of the measurement temperature range) are estimated to be -131 ± 10 kJ·mol⁻¹ (-1.36 eV) and -169 ± 40 J·K⁻¹·mol⁻¹ (-1.75 meV·K⁻¹), respectively. The negative value of ΔH° indicates that the oxygen radical-incorporated state is more stable than the stoichiometric state. Table 1 lists the enthalpy of processes concerning the oxygen radical formation. An equivalent process in the gas phase to eq 1 has a large negative value, -886.5 kJ·mol⁻¹, which principally originates from the instability of O^{2-} in the gas phase. By analogy, the negative ΔH° of oxygen radical formation in C12A7 is due to the instability of the free O^{2-} in the cage. Thus, the free O^{2-} ion is easily oxidized by molecular oxygen. However, the absolute value of ΔH° is smaller than that of the gas-phase reaction. The difference is ascribed to the interaction between the oxide ions and the lattice framework, in which the lattice

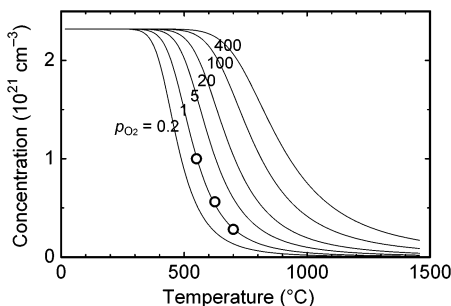


Figure 6. Calculated total equilibrium concentration of the oxygen radicals (O^- and O_2^-) as functions of temperature and partial oxygen pressure. Circles denote the measured total concentration of the oxygen radicals.

strain or Madelung potential of the lattice may play a significant role. Consequently, the free O^{2-} ion is regarded to have an intermediate state between the O^{2-} ion in the gas phase and that in an ordinary metal–oxide lattice.

From eq 5, the total oxygen radical concentration is expressed as function of K and p_{O_2} :

$$[\text{O}_x^-] = \sqrt{K^2 p_{\text{O}_2}^2 + 4Kp_{\text{O}_2}} - Kp_{\text{O}_2} \quad (7)$$

Figure 6 plots the calculated curves for the total oxygen radical concentration, using the values obtained for ΔH° and ΔS° . Here, ΔH° and ΔS° are assumed to be constant since the temperature dependence of ΔH° and ΔS° is generally small.²² The decrease in the equilibrium concentration with temperature is due to the negative ΔS° , which is attributed primarily to the absorption of gas-phase O_2 into the C12A7 lattice during the radical formation (eq 1). Figure 6 also indicates that the range of temperatures for the oxygen radical formation and the O_2 molecule desorption shift to higher temperature as p_{O_2} increases.²²

2. Kinetics of Oxygen Radical Formation. As the oxygen radical formation via eq 1 proceeds, the free O^{2-} ions diffuse from grain interior to the surface to form O^- and O_2^- . Then these radicals diffuse inward. The total diffusion processes are regarded as an uptake of excess oxygen from the atmosphere or chemical inward diffusion of O_2 . Due to the preservation of charge neutrality, the charge flux of the O^{2-} ions must be equal to that of the radical ions. Such ambipolar diffusion²³ is described with a common diffusion coefficient, \tilde{D} .

Next, the total number of the oxygen radicals diffusing into the samples is considered. Since the sample has a porous texture as shown in Figure 2, each grain is approximately a sphere. The total amount of diffusing species, M , entering a sphere with a constant surface concentration is described as²⁴

$$\frac{M}{M_\infty} = 1 - \frac{6}{\pi^2} \sum_{n=1}^{\infty} \frac{1}{n^2} \exp\left(-n^2 \pi^2 \frac{\tilde{D}t}{a^2}\right) \quad (8)$$

where M_∞ corresponds to the equilibrium value for M , and a is the radius of the sphere (half of grain size). The initial change of M/M_∞ against time is approximated to be

$$\frac{M}{M_\infty} \cong \frac{6}{\sqrt{\pi}} \left(\frac{\tilde{D}t}{a^2}\right)^{1/2} \quad (9)$$

giving the power law with an exponent of $1/2$. The constant surface concentration corresponds to the situation where the oxygen radical concentration at grain surfaces is in equilibrium

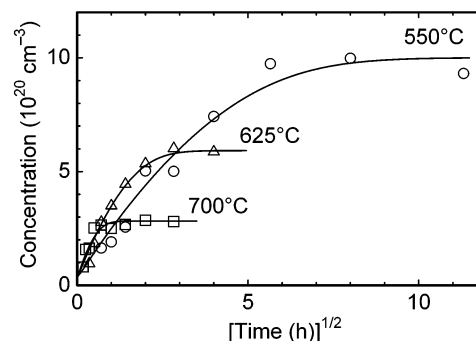


Figure 7. Plot of the total oxygen radical concentration against the square root of the annealing time. Solid lines denote the best fitted curves for eq 8.

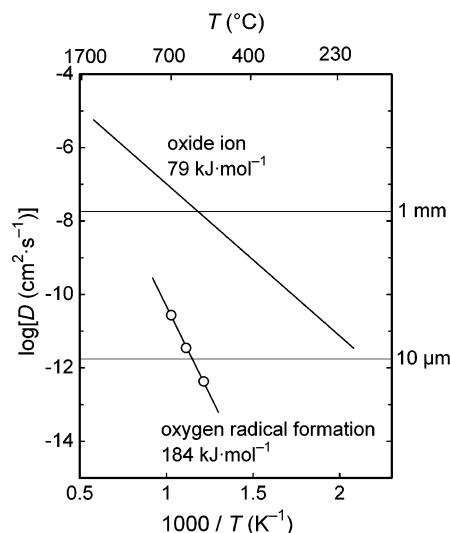


Figure 8. Arrhenius plot of diffusion coefficient (D) in the total ambipolar diffusion process for forming the oxygen radicals. The diffusion coefficient of the oxide ion was estimated from ionic conductivity data (ref 2). The maximum grain sizes for equilibration within 1 day are indicated on the right axis.

during the isothermal annealing. In this case, the flux just within the surface as well as at the grain interior is controlled by the bulk diffusion. If the surface reaction controls the flux just within the surface, the initial change in M/M_∞ against time generally obeys the linear law.²⁵ As observed in Figure 4, the initial growth of the total radical concentration at each annealing temperature accords with the power law with $1/2$ rather than 1. Due to the scattering and error of the data, the effect of the surface reaction is not completely ruled out. However, at least influence of the bulk diffusion on oxygen radical formation is expected to be larger than that of the surface reaction.²⁶ Further, the condition of the constant surface concentration is supported by the fact that oxygen molecules are not detected in Raman measurements, although their presence in the grain shell was suggested in very fine powders.¹⁵ Figure 7 shows the fit of eq 8 for the annealing time dependence of the total oxygen radical concentration. Good agreements again support the conclusion that the rate-determining process for the formation of the oxygen radicals is the bulk diffusion process.

Figure 8 is the Arrhenius plot of the diffusion coefficient for the ambipolar diffusion, \tilde{D} , obtained from the fitting results in Figure 7. A similar plot for the oxide ion, $D_{\text{O}^{2-}}$, calculated from the oxide ion conductivity data² by using the Nernst–Einstein equation is also shown in this figure. The two

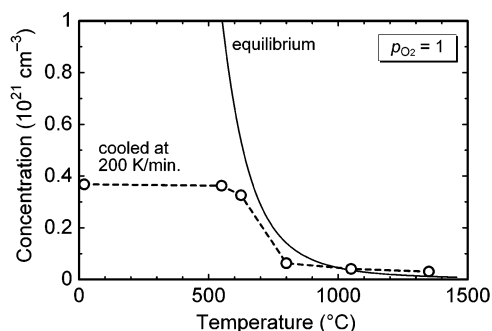


Figure 9. Temperature dependence of the total concentration of the oxygen radicals (O^- and O_2^-) in equilibrium and during cooling with a rate of 200 deg/min from 1350 °C (data are re-plotted from Figure 2 in ref 7).

types of diffusion coefficients are described by the following equations:

$$D_{\text{O}_2^-} = 1.4 \times 10^{-3 \pm 0.1} \exp\left(-\frac{79 \pm 3 \text{ kJ} \cdot \text{mol}^{-1}}{RT}\right) \quad (10)$$

$$\tilde{D} = 2.0 \times 10^{-1 \pm 0.5} \exp\left(-\frac{184 \pm 6 \text{ kJ} \cdot \text{mol}^{-1}}{RT}\right) \quad (11)$$

The \tilde{D} value is smaller by 3–4 orders of magnitude than that of $D_{\text{O}_2^-}$ in the measured temperature range, indicating that the diffusion of oxide ions is not a rate-limiting process for the oxygen radical formation.

Although the diffusion mechanism of anions in the cage has not been examined, a plausible mechanism is either a direct intercage hopping of the anions through a window of the framework or an interexchange between the anion and the framework oxide ions. If the oxygen radicals, O^- and O_2^- , diffuse via the former mechanism, a smaller ionic size is favorable for migration, assuming that both radicals have similar polarizability. Thus, the diffusivity of the O_2^- ion should be smaller than that of the O^- ion. In the latter diffusion process, exchange of O_2^- ions with the framework oxide ions requires complicated processes including the charge transfer between O_2^- and O^{2-} , and the dissociation and rebonding of the O_2^- molecule, thereby significantly suppressing the O_2^- diffusion. In both processes, the diffusivity of O_2^- is expected to be smaller than that of O^- . Since the slowest process determines the total speed of ambipolar diffusion, it is most likely that the measured \tilde{D} is regulated by the diffusivity of O_2^- .

3. Consistency with Data on Samples Cooled from High Temperatures. We previously measured the change in oxygen radical concentration during cooling from 1350 °C in a dry oxygen atmosphere⁸ using sintered compacts that have a similar microstructure to those used in the present study. The data are replotted in Figure 9 along with the calculated equilibrium radical concentration. The total radical concentration during cooling at 200 $\text{K} \cdot \text{min}^{-1}$ is consistent with the equilibrium concentration down to ~ 700 °C, but does not follow the equilibrium concentration below 700 °C. Since the time required to reach equilibrium at ~ 700 °C is on the same time scale as the inverse of the cooling rate, the concentration above ~ 700 °C is expected to equilibrate rapidly. The thermodynamic analysis in the study is consistent with the calculated concentrations. In the lower temperature range, the concentration enhancement is restricted by the steep decrease in the diffusivity. Thus, little change in concentration is observed below ~ 550 °C. In other words, the oxygen radicals are in a very stable state in the low-temperature range.

It is expected that a high concentration of the oxygen radical anions contributes to the ionic current. However, the results of an oxygen concentration cell² concluded that the oxide ion O^{2-} is the only conducting species. Since the concentration cell requires a dense (close-pored) and self-supported (generally ~ 1 mm thick) membrane, the sample in the cell would need a considerable amount of time to reach equilibrium for the incorporating oxygen radicals. For example, the time required for a 1 mm thick sample at 600 °C is as long as $\sim 10^4$ days (1 day for 10 μm , see Figure 8). Thus, the concentration cell measurements may reflect only the higher temperature state. As is demonstrated in Figure 6, the total concentration of oxygen radicals is smaller at higher temperatures. Thus, the results of the concentration cell measurements at lower temperatures do not properly take the oxygen radical ion conduction into account.

V. Conclusion

Oxygen radicals (O_2^- and O^-) in C12A7 are formed mainly through the oxidation of the extraframework O^{2-} ions by absorbed O_2 molecules. The driving force for this process is the instability of the oxide ions in the cage, which is regarded to have an intermediate state between the O^{2-} ion in the gas phase and that in an ordinary metal–oxide lattice. Equilibrium concentration of the oxygen radicals increases as temperature decreases and as the oxygen partial pressure increases. Higher oxygen partial pressure enhances the oxygen radical formation and shifts the O_2 incorporation–desorption to the higher temperature side. The rate-limiting process for the radical formation is the inward diffusion of the oxygen radicals from the surface. Thus, time required for equilibration strongly depends on size of particle or densified bulk. Observed diffusivity for the total radical formation process is most likely regulated by the O_2^- diffusion. The thermodynamic and kinetic analyses demonstrate the high stability of C12A7 encaging a large number of the O^- and O_2^- radicals below ~ 700 °C.

Acknowledgment. This work was supported by the Grant-in-Aid for Creative Scientific Research (No. 16GS0205) from the Japanese Ministry of Education, Culture, Sports, Science and Technology.

References and Notes

- (1) Bartl, H.; Scheller, T. N. *Jb. Miner. Mh.* **1970**, *35*, 547–552.
- (2) Lacerda, M.; Irvine, J. T. S.; Glasser, F. P.; West, A. R. *Nature* **1988**, *332*, 525–526. Irvine, J. T. S.; Lacerda, M.; West, A. R. *Mater. Res. Bull.* **1988**, *23*, 1033–1038.
- (3) Nurse, R. W.; Welch, J. H.; Majumdar, A. J. *Trans. Br. Ceram. Soc.* **1965**, *64*, 323–332. Imlach, J. A.; Glasser, L. S. D.; Glasser, F. P. *Cem. Concr. Res.* **1971**, *1*, 57–61. Zhmoldin, G. I.; Chatterjee, A. K. *Cem. Concr. Res.* **1984**, *14*, 386–396. Edmonds, R. N.; Majumdar, A. J. *Cem. Concr. Res.* **1988**, *18*, 473–478.
- (4) Jeevaratnam, J.; Glasser, F. P.; Glasser, L. S. D. *J. Am. Ceram. Soc.* **1964**, *47*, 105–106.
- (5) Hosono, H.; Abe, Y. *Inorg. Chem.* **1987**, *26*, 1192–1195. Stösser, R.; Nofz, M.; Gessner, W.; Schröter, C.; Kranz, G. J. *Solid State Chem.* **1989**, *81*, 152–164.
- (6) Hayashi, K.; Hirano, M.; Matsuishi, S.; Hosono, H. *J. Am. Chem. Soc.* **2002**, *124*, 738–739.
- (7) Hayashi, K.; Li, Q.; Nishioka, M.; Matsuishi, S.; Torimoto, Y.; Hirano, M.; Sadakata, M.; Hosono, H. *Electrochem. Solid-State Lett.* **2002**, *5*, J13–J16.
- (8) Hayashi, K.; Matsuishi, S.; Ueda, N.; Hirano, M.; Hosono, H. *Chem. Mater.* **2003**, *15*, 1851–1854.
- (9) Hayashi, K.; Matsuishi, S.; Kamiya, T.; Hirano, M.; Hosono, H. *Nature* **2002**, *419*, 462–465.
- (10) Matsuishi, S.; Toda, Y.; Miyakawa, M.; Hayashi, K.; Kamiya, T.; Hirano, M.; Tanaka, I.; Hosono, H. *Science* **2003**, *301*, 626–629.

- (11) Lemonidou, A. A.; Vasalos I. A. *Appl. Catal.* **1989**, *54*, 119–138.
Pant, K. K.; Kunzru, D. *Ind. Eng. Chem. Res.* **1997**, *36*, 2059–2065.
- (12) (a) Li, Q.; Hayashi, K.; Nishioka, M.; Kashiwagi, H.; Hirano, M.; Torimoto, Y.; Hosono, H.; Sadakata, M. *Appl. Phys. Lett.* **2002**, *80*, 4259–4261. (b) Li, Q.; Hayashi, K.; Nishioka, M.; Kashiwagi, H.; Hirano, M.; Torimoto, Y.; Hosono, H.; Sadakata, M. *Jpn. J. Appl. Phys.* **2002**, *41*, L530–L532. (c) Li, Q.; Hosono, H.; Hirano, M.; Hayashi, K.; Nishioka, M.; Kashiwagi, H.; Torimoto, Y.; Sadakata, M. *Surf. Sci.* **2003**, *527*, 100–112.
- (13) Hayashi, K.; Hirano, M.; Hosono, H. *Mater. Integr.* **2003**, *16* [8], 55–59 (in Japanese).
- (14) Unpublished work.
- (15) Yang, S.; Kondo, J. N.; Hayashi, K.; Hirano, M.; Domen, K.; Hosono, H. *Chem. Mater.* **2004**, *16*, 104–110.
- (16) Lunsford J. H. *Catal. Rev.* **1973**, *8*, 135–157. Che, M.; Tench, A. J. *Adv. Catal.* **1982**, *31*, 77–133.
- (17) Che, M.; Tench, A. J. *Adv. Catal.* **1983**, *32*, 1–148.
- (18) Celotta, R. J.; Bennett, A.; Hall, J. L.; Siegel, M. W.; Levine, J. *Phys. Rev.* **1972**, *A6*, 631.
- (19) Chase, M. W., Jr.; Curnutt, J. R.; Downey, J. R., Jr.; McDonald, R. A.; Syverud, A. N.; Valenzuela, E. A. *J. Phys. Chem. Ref. Data* **1982**, *11*, 695.
- (20) Branscomb, L. M.; Burch, D. S.; Smith, S. J.; Geltham, S. *Phys. Rev.* **1958**, *111* 504.
- (21) Atkins, P. W. *Physical Chemistry*, 4th ed.; Freeman: New York, 1990; Chapter 2.6.
- (22) The error of estimated values in Figure 6 becomes larger at the far outside of the measurement temperature range (550–700 °C) due to the small temperature dependence of ΔH° and ΔS° as well as in higher p_{O_2} due to discrepancy from the ideal gas.
- (23) Chiang, Y.-M.; Birnie, D.; Kingery, W. D. *Physical Ceramics*; Wiley: New York, 1997; p 236.
- (24) Crank, J. *The Mathematics of Diffusion*, 2nd ed.; Oxford Science Publications: Oxford, UK, 1975; p 91.
- (25) Exact solution of the diffusion equation is given in ref 24 by assuming that surface concentration is not constant and the flux across the surface is proportional to the difference between the actual concentration just within the surface and the concentration in equilibrium with the surrounding atmosphere. In this case, the value of M/M_∞ has initially linear dependence on time.
- (26) If the surface reaction controls slightly the flux across the surface, the evaluation of the diffusion constant from eq 8 involves an underestimation. In this case, evaluated \tilde{D} in Figure 8 gives a lower limit of the exact diffusivity.